

Low thermal conductivity in bournonite PbCuSbS₃: A comprehensive study

Esteban Zuñiga-Puelles^{1,2}, Raul Cardoso-Gil,² Ayberk Özden³, Nebahat Bulut³, Volodymyr Svitlyk,^{4,5} Cameliu Himcinschi³, Jens Kortus³ and Roman Gumeniuk^{1,*}

¹*Institut für experimentelle Physik, TU Bergakademie Freiberg, Leipziger Straße 23, 09596 Freiberg, Germany*

²*Max-Planck-Institut für chemische Physik fester Stoffe, Nöthnitzer Straße 40, 01187 Dresden, Germany*

³*Institut für theoretische Physik, TU Bergakademie Freiberg, Leipziger Straße 23, 09596 Freiberg, Germany*

⁴*Helmholtz-Zentrum Dresden-Rossendorf, Institute of Resource Ecology, Bautzner Landstraße 400, 01328 Dresden, Germany*

⁵*The Rossendorf Beamline at ESRF, CS 40220, 38043 Grenoble, Cedex 9, France*



(Received 8 July 2022; revised 18 October 2022; accepted 24 October 2022; published 7 November 2022)

Two natural bournonite specimens have been characterized by structural, chemical, spectroscopical, magnetic, and thermodynamic analyses. This study confirms a stoichiometric composition of PbCuSbS₃ and the crystal to be of an outstanding quality allowing us to consider its properties as being intrinsic for this material. Electronic structure calculations, electrical resistivity measurements, and spectroscopical characterizations reveal PbCuSbS₃ to be a direct *n*-type semiconductor with an optical energy gap $E_g^{\text{opt}} = 1.69$ eV, huge Seebeck coefficient and electrical resistivity (e.g., $\sim -1200 \mu\text{V K}^{-1}$ and $\sim 1000 \Omega \text{ m}$ at room temperature, respectively). The thermal conductivity in PbCuSbS₃ is found to be very low [$\kappa(T) \sim 2\text{--}0.5 \text{ W m}^{-1} \text{ K}^{-1}$ in the temperature range 100–600 K] and is dominated by optical phonons ($T > 100$ K), which poorly transport heat, strongly scatter the acoustic ones and substantially intensify the phonon-phonon *unklapp* processes. Additionally, large atomic displacement parameters and the presence of low-energy optical phonons have been identified, evidencing “rattling” effects associated to Cu and Pb atoms in the crystal structure. All these result in high Grüneisen parameters ($\gamma_G = 4.8\text{--}3.2$) and very short phonon mean free path ($l_{\text{ph}} = 11\text{--}3 \text{ \AA}$ for 100–300 K). Thus, the low thermal conductivity in bournonite reflects a combination of different factors leading to a huge phonon anharmonicity.

DOI: [10.1103/PhysRevB.106.195201](https://doi.org/10.1103/PhysRevB.106.195201)

I. INTRODUCTION

Semiconductors with low thermal conductivity (κ) [1] have found applications in the development of thermal isolators and coatings [2], photovoltaic cells (PV) [3], optoelectronic devices or thermoelectric generators (TEG) [4–6]. In general, the thermal transport in a crystalline material is considered as to be mainly mediated by electrons and/or by the quasi-particles arising from lattice vibrations, which are known as phonons [7,8]. The electronic part of the thermal conductivity (κ_{el}) is inversely proportional to the electrical resistivity (ρ) and could be directly calculated from the Wiedemann-Franz law: $\kappa_{\text{el}} = \rho^{-1} L_0 T$, with Lorenz number $L_0 = 2.44 \times 10^{-8} \text{ W } \Omega \text{ K}^{-2}$, which is slightly dependent on the charge carrier concentration in semiconductors. Obviously, contribution of κ_{el} to heat transport in materials with high electrical resistivity is negligibly small and thus heat transport is mediated almost completely by phonons (i.e., κ_{ph}).

Steady progress in the theoretical understanding of the problems of many-body interactions and of strong correlations among the energy carriers, observed over the past few decades, has significantly contributed to $\kappa(T)$ simulations, thus enabling design of solids with targeted properties [1,7,9]. Additionally, the impacts of phonon-dislocations interactions

[10,11], of many-phonon [12] as well as exceptionally strong phonon [13] scatterings on $\kappa(T)$ and even thermal transport beyond the phonon picture [14] are discussed in the literature.

It has been shown that nonmetallic crystals are characterized by low phononic thermal conductivity if they reveal: (i) high atomic mass; (ii) weak interatomic bonding (fulfillment of both these conditions would indicate low Debye temperature, θ_D); (iii) complex crystal structure (number of atoms per primitive unit cell should be ≥ 2 resulting in the appearance of optical branches in the phonon dispersion, which contribute very little to heat transport due to their small group velocities); and (iv) high anharmonicity (i.e., high Grüneisen parameter γ_G , which gives relation of the vibrational frequencies with unit-cell volume changes) [15]. Numerous natural and synthetic pnictides and chalcogenides (e.g., SnSe [16], CaZrSe₃ [17], ZnSb [18], Cu₄Sn₇S₁₆ [19], TlInTe₂ [20], etc.) fulfill these requirements and thus are characterized by low thermal conductivities. Further factors leading to a κ_{ph} reduction in these materials are found in their enhanced phonon anharmonicity, originating from point defects, boundary scattering, rattling effects, bonding inhomogeneity, resonant bondings, among others [1,7,9,21–23].

Naturally occurring bournonite with chemical formula PbCuSbS₃ is a sulfosalt commonly found in hydrothermal systems [24,25] and crystallizes with a noncentrosymmetric orthorhombic crystal structure (space group *Pnm2*₁) [26]. It is reported to melt congruently at 1125 K [27] or to decompose

*roman.gumeniuk@physik.tu-freiberg.de

at 785 K [28]. A theoretical study showed this mineral to be a *p*-type semiconductor [29] and energy gaps of 0.69 eV [28,29] or 1.41 eV [30] were obtained from the calculated electronic structure, or with $E_g = 1.22$ eV [31], as observed from optical calculations. There were numerous attempts to estimate the energy band gap of PbCuSbS₃ applying spectroscopic methods, which result in $E_g \approx 1.2$ – 1.3 eV [32–35] and 1.55 eV [36]. Studying the electrical transport properties of a synthetic bournonite, the so-called bipolar effect was observed [37] (i.e., by increasing temperature the conductivity changes from semiconducting to metallic-like at ~ 560 K), as well as positive Seebeck coefficients (i.e., *p*-type semiconductor). A synthetic sample is also found to be a diamagnet [32]. Additionally, the interest in naturally occurring and synthetic chalcogenides is triggered by their interesting properties for possible semiconductor applications [38–48].

The most spectacular property of PbCuSbS₃ is its very low phonon-mediated thermal conductivity (i.e., $\kappa \sim 0.5$ – 2 W m⁻¹K⁻¹ in the temperature range 100–300 K) [28]. The analysis of the chemical bonding situation based on the electron localization function (ELF) calculations attributed the low κ in bournonite to the presence of lone-pair electrons on Pb²⁺ and Sb³⁺ ions [28]. Therein, they are believed to contribute to the electrostatic repulsion between the *s*-electron distributions of neighboring atoms, as a source of anharmonic phonon scattering. The low thermal conductivity of the bournonite triggered studies of its possible application in PVs [30,31,33–36] and TEGs [29]. However, both of them failed due to impossibility to achieve a good crystallinity in the thin films and therefore a rather high electrical resistivity, respectively. Nevertheless, there are many routes to optimize the synthesis of bournonite thin films as well as to tune its electrical transport properties, which make this material still promising on both respects.

In this paper we report on the magnetic, thermodynamic, spectroscopic, electrical and thermal transport properties of well established poly- and single crystalline natural bournonites specimens. A combined theoretical and experimental study allowed us to clearly estimate intrinsic characteristics of this material as well as to shed light on the dominant physical mechanisms leading to the low thermal conductivity in the mineral.

II. EXPERIMENTAL

Natural poly- and single crystalline samples originating from mines in Neudorf im Harz (Germany) and Vibora (Bolivia) (further referred in text as sample #1 and #2, respectively) were selected after prior analysis using an optical microscope.

Further, they were characterized by powder- (PXRD) and single crystal x-ray diffraction (SCXRD). The PXRD patterns were collected on an image plate Guinier camera Huber G670 (Cu- $K\alpha_1$ radiation, $\lambda = 1.540562$ Å, $5^\circ \leq 2\theta \leq 100^\circ$, $\Delta\theta = 0.005^\circ$). Temperature dependent synchrotron PXRD measurements ($\lambda = 0.61992$ Å) were performed at the beamline BM20 of the European Synchrotron Radiation Facility (ESRF, Grenoble, France). The sample was enclosed in a quartz-capillary of 0.3 mm under Ar atmosphere. The temperature control was performed using a gas blower calibrated with Ag as standard. Phase analysis was carried out with

WinXpow program package [49]. The SCXRD data were collected on a Bruker D8 Tornado diffractometer, equipped with a PHOTON area detector and Mo- $K\alpha$ radiation ($\lambda = 0.71073$ Å). The data analysis and image integration were performed with the CrysAlisPro software [50]. Both PXRD and SCXRD crystal structure refinements were performed using the WinCSD program package [51].

The chemical analysis by inductively coupled plasma-optical emission spectroscopy (ICP-EOS) was performed with an ICP-EOS 5100 equipment (Agilent Technologies). The obtained total chemical compositions of both specimens are presented in Table S4 in Supplemental Material [52]. This study confirms the stoichiometric composition PbCuSbS₃ as well as a small impurity amount in bulk material (i.e., <1 wt.%), which is not detectable by PXRD.

A representative area of the samples #1 and #2 were embedded in a conductive resin, grinded and polished. The final polishing was performed with 0.25 μm diamond powder. The obtained surfaces were analyzed by scanning electron microscopy (SEM) and spectroscopic ellipsometry. Local chemical composition and microstructure analyses were carried out using a SEM-JEOL JSM 7800F microscope equipped with Bruker Quantax 400, XFlash 6||30 (silicon drift detector) EDXS spectrometer. This study confirmed again both minerals to be single phase and with the stoichiometric composition PbCuSbS₃ (Table S4 in Supplemental Material [52]). The only difference between the samples was that the surface of the specimen #1 revealed numerous cracks and fluid inclusions (“bubbles”) (Fig. S1 in Supplemental Material [52]), which are characteristic of the minerals of hydrothermal origin [53].

Low temperature (LT, $T \leq 300$ K) magnetic susceptibility [$\chi(T)$] and specific heat capacity [$c_p(T)$] were measured with VSM and HC modules of DynaCool-12 from Quantum Design.

High temperature (HT, $300 \text{ K} \leq T \leq 600 \text{ K}$) electrical resistivity $\rho(T)$ and Seebeck coefficient $S(T)$ were obtained on a ULVAC ZEM-3, whereas thermal diffusivity [$D(T)$] was measured via Laser Flash Method (LFA 457 MicroFlash, Netzsch). The thermal conductivity was calculated according to: $\kappa(T) = D(T)c_p d$, where d is the density.

Spectroscopic ellipsometry was performed on polished samples at 55°, 60° and 65° incidence angles, in the 0.73–6 eV range using an M2000 J.A. Woollam ellipsometer.

Nonpolarized Raman spectra were collected with a Horiba LABRAM System-HR-800 (CCD camera, 600 grooves per mm grating, HeNe laser 633 nm, 50X objective N.A of 0.5). Initial spectrometer calibration was performed with Si[111]-standard by use of its 520.6 cm⁻¹ peak. Neon calibration-lamp spectra were recorded after each measurement to track and correct any shift during the Raman measurements. Temperature-dependent Raman spectra and Raman thermal conductivity were obtained with a Linkam THMS-600 cooling-heating stage. The stage was continuously cooled by liquid nitrogen vapor flow between 100 and 400 K and the samples were fixed with silver paste to the stage, to prevent sample drift and to provide better thermal contact.

Optothermal Raman (OTR) technique was utilized to get Raman thermal conductivity between 100 and 400 K [54–56]. The Raman spectra at each temperature were recorded by

performing a series of measurements with different absorbed excitation powers (e.g., 6.5, 45, and 400 μW). The smallest absorbed excitation power was used as calibration curve (thermometer) and thermal conductivity was obtained from the Eq. (1) [56],

$$\kappa = \frac{\frac{d\Delta w}{dT}}{4s\sqrt{\pi}\frac{d\Delta w}{dP}} \quad (1)$$

where $s = 1.5 \mu\text{m}$ is the laser spot size on the sample, $d\Delta w/dT$ ($\text{cm}^{-1} \text{K}^{-1}$) is the slope of the calibration curve and $d\Delta w/dP$ ($\text{cm}^{-1} \text{W}^{-1}$) is the slope of power-dependent Raman peak shift (Fig. S2 in Supplemental Material [52]). Absorbed power was obtained by multiplying the laser power (after objective) by an absorption value of 0.65 (at 633 nm), obtained from ellipsometry measured extinction coefficient and refractive index.

Electronic structure for bournonite within the generalized gradient approximation (GGA) of the density functional theory (DFT) was calculated using the full-potential FPLO code (version 18.00-52) [57]. This scalar relativistic calculation was performed using the exchange-correlation functional by Perdew and Wang [58]. The k mesh included $12 \times 12 \times 12$ points in the first Brillouin zone. The energy dependent dielectric tensor (ϵ_{ij} with $i, j = x, y, z$) is composed of intra- and interband contributions. They are obtained from the Drude-model with plasmon frequencies originating from electronic structure calculations and the DFT-calculated imaginary part of the dielectric function (ϵ_2), respectively. The symmetry analysis of the ϵ_{ij} function revealed a negligible optical anisotropy, thus its real (ϵ_1) and imaginary (ϵ_2) parts correspond to the average from all symmetry directions.

Elastic constant calculations of bournonite were performed using the Quantum-Espresso code [59], based on plane waves and pseudopotentials [60]. For the exchange-correlation functional the Perdew-Burke-Ernzerhof (PBE) [61] one has been used together with the projector augmented wave (PAW) method. The plane wave cut-off has been fixed to 90 Rydberg based on convergence tests. For the Brillouin zone sampling a Monkhorst-Pack grid [62] with $8 \times 8 \times 8$ k points including the origin was chosen. There are nine independent elastic constants due to the symmetry of the space group, which are further referred as C_{11} , C_{22} , C_{33} , C_{44} , C_{55} , C_{66} , C_{23} , C_{12} , and C_{13} . These elastic constants are represented in Voigt notation. To calculate the elastic constants, C_{ij} , this requires properly chosen distortions of the unit cell, which can be represented by nine distortion matrices \mathbf{D}_{ij} describing the distortion of the unit cell. The amount of distortion was controlled by numerical value in the range of -0.05 to 0.04 [63].

III. RESULTS AND DISCUSSION

A. Crystal structure

A small crystal suitable for x-ray diffraction (SCXRD) measurement was mechanically extracted from the crashed piece of sample #2. The obtained data set could be indexed with the orthorhombic unit cell parameters (UCP) given in Table I. The observed reflection conditions for $0kl$ with $k+l=2n$, $0k0$ with $k=2n$ and $00l$ with $l=2n$ indicate two possible space groups: $Pnm2_1$ and $Pnmm$. This fact as

TABLE I. Crystallographic data for the single crystal refinement of PbCuSbS_3 .

Sample	#2
Refined composition	PbCuSbS_3
Space group	$Pnm2_1$ ($N^\circ 31$)
From PXRD a (\AA)	7.8060(8)
From PXRD b (\AA)	8.1479(8)
From PXRD c (\AA)	8.7017(9)
Radiation, λ (\AA)	$\text{Mo-K}\alpha$, 0.71073
Calculated density d (g cm^{-3})	5.8694
Scan; step ($^\circ$); N (images)	ϕ and Ω ; 1; 2021
Maximal 2Θ ($^\circ$)	61.4
Ranges in h, k, l	$-11 \leq h \leq 11$ $-11 \leq k \leq 11$ $-12 \leq l \leq 12$
Absorption correction	Numerical
$T(\text{max})/T(\text{min})$	1.00/0.55
Absorption coeff. (mm^{-1})	39.68
$N(\text{hkl})$ measured	44587
$N(\text{hkl})$ unique	940
R_{int}	0.025
$N(\text{hkl})$ observed	43739
Observation criterion	$F(\text{hkl}) \leq 4\sigma(F)$
Refined parameters	64
$R_F; R_W$	0.023; 0.032
Residual peaks ($e \text{\AA}^{-3}$)	$-1.56/1.87$

well as the observed dimensions of UCPs prompted us to use for the further refinement the structural model reported for bournonite in the space group $Pnm2_1$ ($N^\circ 31$) [26]. The refinement converged with low values of reliability factors (Table I), atomic coordinates and anisotropic displacement parameters listed in Table S2 in Supplemental Material [52]. The refined crystal structure fit well with earlier reported models for bournonite [26,28,33,64]. We also used the values from Tables I and S5 to perform Rietveld refinement of our powder XRD data. The refined profiles are given in Fig. 1.

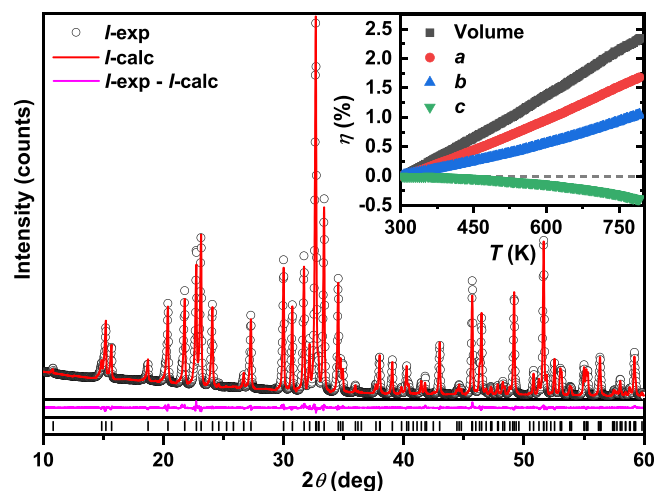


FIG. 1. PXRD pattern and Rietveld refinement for sample #2. Inset: Temperature dependent unit-cell parameter increments (η) in %, after synchrotron data.

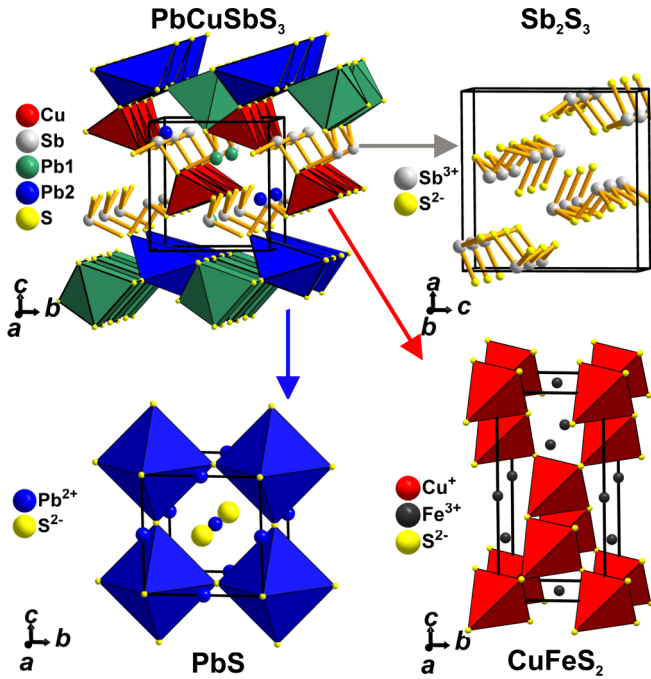


FIG. 2. Arrangement of the coordination polyhedra in the crystal structures of bournonite ($\text{PbCuSb}_3\text{S}_3$), stibnite (Sb_2S_3), galena (PbS), and chalcopyrite (CuFeS_2).

The facts that all observed intensities could be quantitatively described (i.e., no impurity phases are observed in agreement with performed chemical and EDX analyses) and the refinement converged with low reliability factors (i.e., $R_I = 5.5\%$ and $R_P = 4.0\%$) validate the used structural model.

The temperature dependent synchrotron PXRD up to 925 K performed on $\text{PbCuSb}_3\text{S}_3$ revealed almost linear increase of UCPs a and b with the temperature, whereas the c parameter decreases. The relative thermal expansion (η , %) (Fig. 1 inset) is of 1.7%, 1.1%, -0.4% , and 2.4% for a , b , c , and unit cell volume V , respectively in the temperature range 300–800 K. The observed volumetric η values are typical for the majority of the intermetallic compounds [8]. Interestingly, earlier studies reported for bournonite melting points at 633 K (for hydrothermally synthesized nanocrystalline sample) [32] or 785 K [28], and 1125 K [27] for synthetic bulk specimens. In this paper, we could index PXRD patterns with orthorhombic bournonite UCPs up to 800 K and above this temperature peaks belonging to its structure could not be identified. Considering a broad maximum in the recorded profile, which is obviously due to an amorphous phase, we came to the conclusion, that the sample began to react with the quartz capillary at $T > 800$ K, and thus bournonite is thermally stable only up to this temperature.

The arrangement of the coordination polyhedra in the crystal structure of bournonite is presented in Fig. 2. $[\text{CuS}_4]$ tetrahedra and $[\text{SbS}_3]$ fragments are similar to those occurring in the chalcopyrite CuFeS_2 and stibnite Sb_2S_3 . Even more, as one can see from Table II the interatomic contacts $d_{\text{Cu-S}}$ and $d_{\text{Sb-S}}$ are in agreement with those reported in literature for the corresponding minerals (i.e., 2.3 Å and 2.45 Å, respectively) [65,66]. Taking into account that the interatomic distances are

TABLE II. Interatomic contacts d with sulfur in the crystal structure of $\text{PbCuSb}_3\text{S}_3$.

Atom		d , Å	Atom		d , Å
Pb1	–1S1	2.7947(6)	Cu	–1S2	2.285(1)
	–2S3	2.8832(6)		–1S1	2.335(1)
	–2S3	3.1811(7)		–1S4	2.342(1)
	–2S4	3.3431(5)		–1S3	2.416(1)
Pb2	–1S2	2.7964(7)	Sb1	–2S4	2.4613(5)
	–2S4	2.7995(5)		–1S1	2.4631(8)
	–1S1	3.1021(7)	Sb2	–1S2	2.4365(6)
	–2S3	3.4713(5)		–2S3	2.4609(6)

close to the sums of ionic radii for a respective coordination number (CN) [$r_{(\text{Cu}^{1+})} = 0.6$ Å, $r_{(\text{Sb}^{3+})} = 0.76$ Å for CN = 4 and $r_{(\text{S}^{2-})} = 1.84$ Å for CN = 6] one can assume Cu and Sb ions to be in the oxidation state 1+ and 3+, respectively [67]. On the other hand, $[\text{Pb}_2\text{S}_6]$ octahedron with strongly shifted vertices and a mono single capped trigonal prism $[\text{Pb}_1\text{S}_7]$ differ from an ideal structural unit occurring in the structure of galena (PbS) (Fig. 2) [68]. Such a difference is also reflected in the interatomic distances. So, if in galena PbS $d_{\text{Pb-S}}$ is of 2.967 Å and thus very close to the sums of ionic radii [i.e., $d_{\text{Pb}^{2+}-\text{S}^{2-}} = 3.03$ Å], in bournonite it is $\sim 8\%$ shorter. With this respect our study agrees well with reported values [28,32,33,64]. However, this finding could also indicate the oxidation state of Pb atoms in the crystal structure of $\text{PbCuSb}_3\text{S}_3$ to be larger than 2+. This simple structural analysis would be in contradiction with the widely accepted $[\text{Pb}^{2+}][\text{Cu}^{1+}][\text{Sb}^{3+}][\text{S}^{2-}]_3$ ionic formula [28,29], thus indicating that this point requires further careful studies.

The crystal structure of bournonite is also characterized by numerous empty voids. The calculation of the so-called “packing index” (pi), using Platon software [69], indicated only $\sim 80\%$ of the structural arrangement to be filled. This index is comparable with pi of such prominent cage compounds as, e.g., tetrahedrite ($\text{Cu}_{12}\text{Sb}_4\text{S}_{13}$) ($pi \approx 64\%$) [70,71] or Chevrel phase (Mo_3S_4) ($pi \approx 78\%$) [72], which assumes a strong phonon scattering due to rattling effects and thus a lowered thermal conductivity [7,73,74].

B. Electronic structure

The electronic density of states (DOS) calculated for bournonite based on the structural data given in Tables I and S5 is presented in Fig. 3. The DOS is reminiscent of those reported in [28–30]. The valence band consists of three regions: (i) a low-lying extending from ~ -14.5 eV to -12.3 eV, which is mainly due to S-3s states; (ii) an intermediate (~ -9.3 eV to ~ -7.1 eV) composed of Pb-6s, S-3p and Sb-5s; and finally (iii) a high-energy one ranging from ~ -5.7 eV up to Fermi level E_F and being due to the contribution of generally S-3p and Cu-3d electrons. The valence and conduction bands in the electronic structure of $\text{PbCuSb}_3\text{S}_3$ are separated by an energy gap $E_g = 0.5$ eV, which is by a factor of ~ 3 lower than the spectroscopically estimated one (see discussion below). The tendency of the density functional theory (DFT) to underestimate the E_g is discussed elsewhere [8,75,76]. The fact that Pb-6p, Cu-4s, and Sb-5p states are almost depopulated (i.e.,

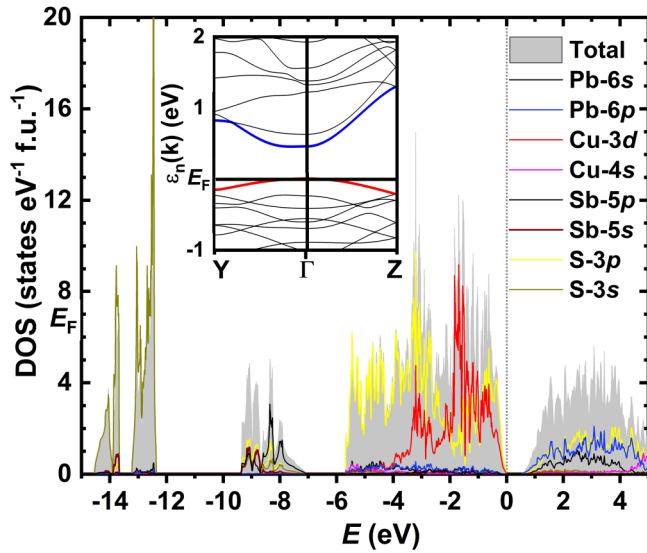


FIG. 3. The total and atomic resolved electronic density of states for PbCuSbS₃. Inset: The band structure of bournonite.

are situated in conduction band) (Fig. 3) would confirm the positive charges of these ions in agreement with the observed structural peculiarities (see analysis above) and previous study [77].

The calculated band structure of bournonite (Fig. 3 inset) reveal it to be a direct semiconductor, since the valence band maximum (VBM, red line in Fig. 3 inset) and conduction band minimum (CBM, blue line in Fig. 3 inset) are in front of each other close to the Γ point. As it is reported earlier, accounting for the spin-orbit coupling (SOC) is leading to an indirect gap together with its reduction by a factor of ~ 2 (i.e., $E_g = 0.385$ eV) [28].

C. Magnetic and thermodynamic properties

The temperature dependencies of magnetic susceptibility $\chi(T)$ corrected by diamagnetic increments [77,78] for both samples are presented in Fig. 4 (inset). In contrary to the previous report [32], where synthetic bournonite is found to be a diamagnet, we observe a weak Pauli paramagnetism in the natural specimens. Interestingly, if one would correct the magnetic susceptibility of a synthetic specimen by diamagnetic increments, it would also reveal a weak Pauli paramagnetism [32]. $\chi(T)$ is nearly the same and temperature independent for both studied specimens down to ≈ 125 K and then shows a strong upturn, which obviously can be attributed to Fe-minor admixture or As impurities in samples #1 and #2, respectively (Table S4 in Supplemental Material [52]).

The temperature dependencies of the specific heat for both studied bournonites in $c_p/T^3(T)$ presentation (Fig. 4) reveals a clear maximum centered at $T \approx 12$ K followed by a less pronounced shoulder. Such a behavior is known for cage-compounds (e.g., intermetallic clathrates [79], filled skutterudites [80], and Remeika phases [81]), where large vibration of a weakly bounded guest atom incorporated in oversized atomic cage is causing a “rattling” effect. This is leading to the appearance of low-energy optical modes in the phonon spectrum of a material, reflected in a maximum in

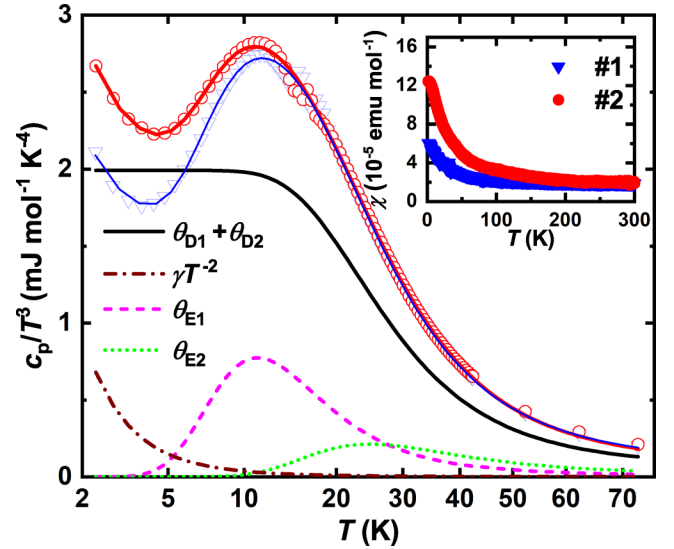


FIG. 4. Temperature dependent specific heat capacity for both specimens in the $c_p/T^3(T)$ presentation, together with fits (solid lines) to Eq. (2). The separate contributions for sample #2 are given as dotted and dashed lines. Inset: temperature dependent magnetic susceptibility after diamagnetic corrections.

$c_p/T^3(T)$ as well as enhanced values of atomic displacement parameters (ADP) of the rattlers (i.e., guest atoms). In the crystal structure of the bournonite latter would be a case for Cu, Pb1, and Pb2 atoms (Table S5 in Supplemental Material [52]). Therefore, we analyzed the measured specific heat applying the model given by Eq. (2) [82,83],

$$C_p(T) = \sum_i C_{Di}(T) + \sum_j C_{Ej}(T) + \gamma T \quad (2)$$

where $C_{Di}(T)$, $C_{Ej}(T)$ and γT stays for the Debye-, Einstein-, and electronic contributions to the specific heat capacity, respectively. In the model, the Debye term should describe the phonon spectrum of the strongly bonded framework whereas the Einstein term is staying for the low-energy optical modes arising from the “rattling” motion. Since bournonite reveal a complex noncentrosymmetric crystal structure, as well as a framework consisting of two sorts of atoms with very different atomic masses (i.e., Sb and S), one could expect that only one Debye contribution would be insufficient to describe such a complicated phonon spectrum. Therefore, in the first fit attempt we assumed $i = 2$. On the other hand, the enhanced ADPs are observed for three metallic atoms (Table S5 in Supplemental Material [52]), which would suggest three “rattling” modes. However, taking into account almost the same ADPs and similar coordination polyhedra for Pb1 and Pb2 we assumed that their contributions are very similar and could be not distinguished. Therefore, two ($j = 2$) $C_{Ej}(T)$ terms (corresponding to Cu and Pb) were included in the fit,

$$C_{(Di)}(T) = 3N_{Di}R \left(\frac{T}{\Theta_{Di}} \right)^3 \int_0^{\Theta_{Di}/T} \frac{x^4 e^x}{(e^x - 1)^2} dx, \quad (3)$$

$$C_{Ej}(T) = N_{Ej}R \left(\frac{\Theta_{Ej}}{T} \right)^2 \frac{e^{\Theta_{Ej}/T}}{(e^{\Theta_{Ej}/T} - 1)^2}. \quad (4)$$

TABLE III. Fit parameters for natural PbCuSbS₃ specimens.

Fit parameter	#1	#2
N_{D1}	10.0(2)	10.0(2)
Θ_{D1} (K)	536(5)	678(4)
N_{D2}	5.3(8)	5.8(4)
Θ_{D2} (K)	131(1)	124(4)
N_{E1}	0.9(2)	0.7(1)
Θ_{E1} (K)	53(2)	55(1)
N_{E2}	2.0(5)	2.2(1)
Θ_{E2} (K)	99(4)	123(1)
γ (mJ mol ⁻¹ K ⁻²)	2.9(3)	3.7(4)

As it is known, total heat capacity $C_p(T)$ as well as its terms $C_{D_i}(T)$ [Eq. (3)] and $C_{E_j}(T)$ [Eq. (4)] are dependent on the numbers of modes: $N_{\text{tot}} = N_{D_i} + N_{E_j}$. Considering the stoichiometry of bournonite one can expect $N_{\text{tot}} = 18$, with $N_{D_i} = 12$ (due to Sb and S atoms) and $N_{E_j} = 6$ (due to Cu and Pb atoms). And indeed, the fit resulted in $N_{\text{tot}} \approx 18$. However, the assignments of the separate modes are deviating from the initial assumption [i.e., $N_{D_i} \approx 15$ –16 and $N_{E_j} \approx 3$ (Table III)]. Seemingly, the phonon spectrum of bournonite is much more complex and does not allow us to achieve the accurate description using the simplified model, which was perfectly working in the case of the Na₂₄Si₁₃₆ clathrate [82].

On the other hand, using the values of ADPs for Cu and Pb atoms presented in Table S5 in Supplemental Material [52], one could calculate the characteristic Einstein temperatures at RT from $U_{\text{iso}} = k_B T / [m(2\pi\nu)^2]$ (with ν and m as the frequency of the “rattling” vibration and the mass of an atom, respectively) and $\Theta_E = h\nu/k_B$. The values $\Theta_E(\text{Cu}) \approx 101$ K and $\Theta_E(\text{Pb}) \approx 62$ –64 K are in good agreement with Θ_{E1} and Θ_{E2} given in Table III. This finding would confirm Cu and Pb atoms to be responsible for the “rattling” effect in bournonite.

The Sommerfeld coefficient γ of the electronic specific heat is different from zero, which might be attributed to the presence of some metallic impurities (Table S4 in Supplemental Material [52]). With this respect the investigated in this work samples should be considered as being much less contaminated in comparison to the specimen studied in [32] (i.e., $\gamma = 10.9$ mJ mol⁻¹K⁻²).

D. Raman spectroscopy

Normalized Raman spectra with respect to most intense peak (324 cm⁻¹) for both natural specimens are shown in Fig. 5. They revealed similar spectral features indicating identical composition and crystallinity, in agreement with XRD and SEM-EDXS characterizations. Experimentally, bournonite’s Raman bands are found between 100 cm⁻¹ and 400 cm⁻¹, demonstrating a broad region below 250 cm⁻¹ and sharper peaks above it. The group theoretical inspection predicts 69 Raman active modes for bournonite ($\Gamma = 20A_1 + 15A_2 + 14B_1 + 20B_2$).

The Raman spectra of sulfides containing XS₃ pyramidal groups (either interlinked or isolated) are dominated by stretching and bending modes [84]. This is correct for a broad range of chalcogenides, such as tetrahedrite-tennantite ($X = \text{As-Sb}$) solid solutions, stibnite ($X = \text{Sb}$), bismuthinite ($X =$

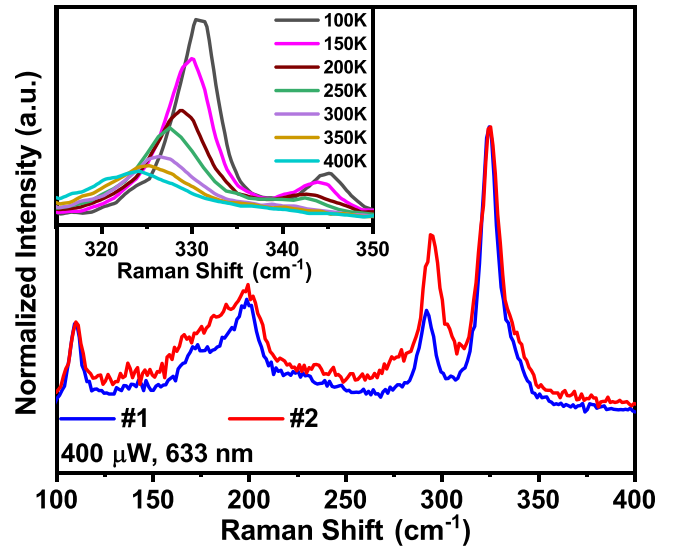


FIG. 5. Room-temperature Raman spectra measured on natural PbCuSbS₃ samples. Inset: Temperature dependence of the strongest peak in Raman spectra for sample #2.

Bi), and bournonite ($X = \text{Sb}$), where the most intense band at 324 cm⁻¹ with a weaker one at 339 cm⁻¹ are assigned to Sb-S stretching [84,85]. The second most prominent Raman band at 292 cm⁻¹ and its shoulder (275 cm⁻¹) are assigned to S-Sb-S bending modes. Interestingly, it has been proposed that Sb units having different average Sb-S distances may result in strong Sb-S stretching modes instead of one Sb-S stretching and one S-Sb-S bending mode [85]. Furthermore, XRD refinements indicating identical (Table I) average Sb-S distances would support the former statement.

E. Spectroscopic ellipsometry

The ellipsometric spectra were fitted using a two-phase model: bulk bournonite/ambient, where the bournonite optical response was described by applying four Gaussian oscillators model, which implies the Kramer-Kronig consistency of the optical constants. The energies of the Gaussian oscillators obtained from the fit were 2.31 eV, 3.01 eV, 4.25 eV, and 7.95 eV. The real (ϵ_1) and imaginary (ϵ_2) parts of the dielectric function obtained from ellipsometry for the sample #2 together with the theoretically calculated are plotted in Fig. 6. They are in good agreement, especially considering that our calculations did not include the Hubbard term (U). Its incorporation is known to improve the electron localization and thus, improves the precision of the estimation of intra- and interbands contributions to the dielectric function [8].

From the experimental and calculated real (ϵ_1) and imaginary (ϵ_2) parts, the optical constants and absorption coefficient of bournonite are determined (see Fig. 7). The optical bandgap E_g^{opt} can be obtained by linear projection of the latter to zero absorption. The experimentally obtained E_g^{opt} values 1.83 eV and 1.69 eV for samples #1 and #2, respectively agree well with the theoretically calculated one of 1.49 eV. The spectroscopic contribution of the fluid inclusions on the studied surface of the specimen #1 lead to an increase of the energy gap by 0.14 eV (see Fig. S1 in Supplemental Material [52]).

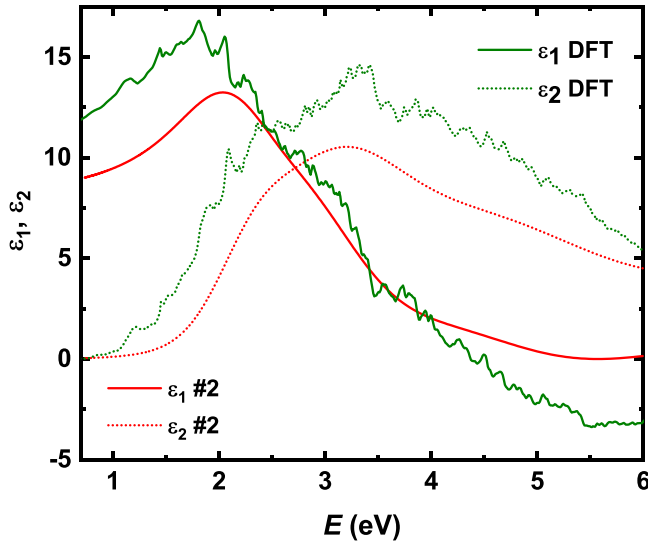


FIG. 6. Comparison of real (ϵ_1) and imaginary (ϵ_2) parts of the dielectric function evaluated from ellipsometry data for sample #2 and obtained from DFT calculation.

Consequently, $E_g^{\text{opt}} = 1.69$ eV is considered as to be representative of the stoichiometric PbCuSbS_3 .

The dielectric function calculated using density functional theory compared with the experimentally determined one shows good agreement of the shape and of the absorption edge. In order to assign the bands seen in ϵ_2 , the electronic density of states was computed. Figure 3 shows the total DOS and the relevant atomic projection of the DOS. The allowed optical transitions should have energies matching the energy difference of the bands involved in the transition. Inspecting the DOS for energy differences around 1.5 eV one finds possible transitions between Cu-3d and Pb-6p. Using the peak

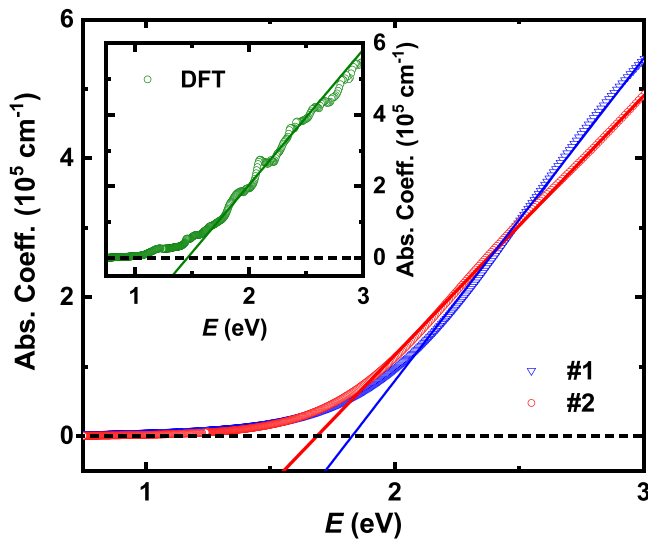


FIG. 7. Experimental absorption coefficients of natural PbCuSbS_3 plotted against photon energy (E). Inset: Theoretically calculated absorption coefficient. The linear extrapolation (continuous lines) to zero absorption (dashed lines) shows the experimental and calculated optical band gaps for bournonite.

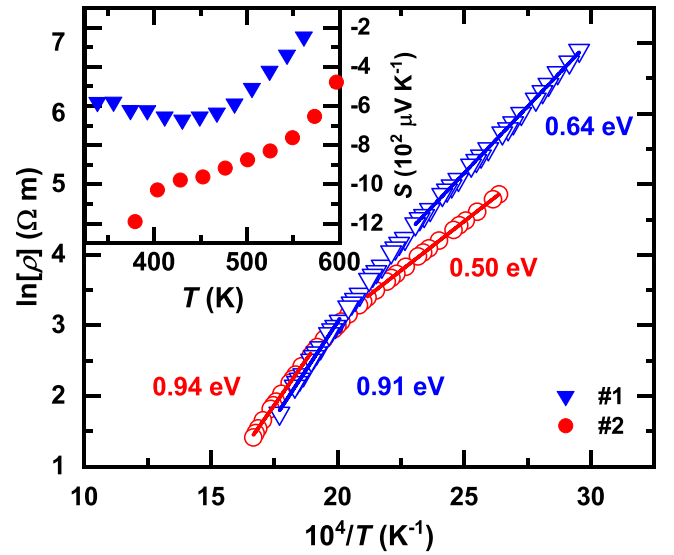


FIG. 8. Temperature dependent electrical resistivity of bournonites in $\ln\rho(T^{-1})$ representation (full lines represent the fits to Eq. (5), with respective energy gaps). Inset: Temperature dependent Seebeck coefficients.

positions in the DOS close to the band gap for these states (Cu-3d at -0.37 eV and Pb-6p at 1.1 eV) one finds indeed an energy difference of ~ 1.49 eV. The optical band gap being larger than the electronic band gap suggests an indirect band gap semiconductor, which seems to be at odds with the band structure shown in Fig. 3. However, this behavior may also be caused by large dipole matrix elements for the interband transition around 1.49 eV dominating the optical spectra in that energy window.

F. Electrical transport

The temperature dependencies of electrical resistivity in the Arrhenius plot and Seebeck coefficient are shown in Fig. 8 and inset therein, respectively. The resistivity of both studied samples varies in the $\sim 10^2$ Ω m range (Table IV) and decreases with increasing temperature as $\rho \propto e^{1/T}$, which indicate a semiconductor-like behavior. This finding is in contradiction to previously reported bipolar effect in a synthetic bulk bournonite [37]. Since the specimen studied there was poorly characterized (neither Rietveld refinement on XRD, nor chemical analysis, or EDX study were performed) one can assume such an effect may originate from a metallic impurity or off-stoichiometry of that sample.

TABLE IV. Electrical transport parameters for PbCuSbS_3 obtained from fits above 500 K.

Sample	E_g^{opt} (eV)	$E_g^{\rho*}$ (eV)	$\rho_0 \times 10^{-4}$ (Ω m)	$\rho^{375\text{K}}$ (Ω m)	PF^{max} ($\mu\text{W m K}^{-2}$)
#1	1.83(1)	0.91(1)	5.6(9)	377	7
#2	1.69(1)	0.94(1)	4.8(8)	128	35

The electrical resistivity was fitted in selected temperature ranges according to the Arrhenius equation,

$$\rho(T) = \rho_0 e^{-E_g^{\rho}/2k_B T} \quad (5)$$

where ρ_0 is the residual resistivity and E_g^{ρ} is the energy gap. The parameters obtained from that fit are collected in Table IV. As expected, the energy gaps E_g^{ρ} are by $\sim 50\%$ smaller in comparison with the optical ones. The Arrhenius plot characterizes the electrical transport band gap (E_g^{ρ}) and assumes it as constant in the fitted temperature range. Our experimental values led to two different ranges, $E_g^{\rho} \sim 0.5$ – 0.64 eV close to RT and ~ 0.94 eV at HT (Fig. 8). The former value would be in agreement with the DFT transport gap with an $E_g \sim 0.5$ eV (Fig. 3), closer to the former one at RT.

From the observed ρ_0 and ρ^{375K} values one could assume a better electrical quality of sample #2. It indicates a larger impurity concentration introducing additional charge carries in the specimen. This finding is in agreement with magnetic susceptibility and specific heat measurements, where crystal #2 is found to reveal higher values of $\chi(T)$ (Fig. 4) and of the Sommerfeld coefficient γ (Table III), respectively.

The absolute $S(T)$ values of sample #1 (inset to Fig. 8) are comparable with that reported for the synthetic bournonite in [37]. Also, negative Seebeck coefficients would imply electrons to be the charge carriers in the mineral and not holes as it is shown in the previous experimental [37] and theoretical [29] studies. Interestingly, the DFT simulations reported in [29] resulting into p -type conductivity were based on the energy optimization of the possible formation of hole-like defects/vacancies in the crystal structure. Hence, two scenarios became possible: (i) the electron-mediated type of electrical transport should hint towards absence of such defects in the here studied samples or (ii) DFT is strongly underestimating the formation energies of the structures with Pb vacancies as well as with Pb atoms substituted by Cu. Considering the relations $|S| \propto n^{-1}$ and $\rho \propto n^{-1}$ one has also to conclude, a rather low charge carrier concentration (n) in the bournonite, which is typical for a nondoped semiconductor.

To estimate the TE efficiency of the studied samples, the so-called power factor $PF = S^2 T \rho^{-1}$ is calculated. Its maximal values are presented in Table IV. They are by nearly three orders of magnitude lower than those of the state-of-the-art materials [86]. Obviously, a tuning of electrical transport properties (electron/hole doping aiming the enhancement of charge carrier concentration/mobility) is needed to improve the TE performance of the bournonite.

G. Thermal transport

The temperature dependencies of the thermal conductivity $\kappa(T)$ for both studied specimens obtained by LFA and OTR techniques are presented in Fig. 9. They are nearly the same and agree well with earlier reports for synthetic bournonite [28]. Since the electronic contribution to $\kappa(T)$ [obtained from the Wiedemann-Franz law: $\kappa_{el} = L_0 T / \rho(T)$, where $L_0 = 2.44 \times 10^{-8} \text{ W } \Omega \text{ K}^{-2}$ is the Lorenz number] is found to be negligibly small (i.e., $\kappa_{el} < 10^{-6} \text{ W m}^{-1} \text{ K}^{-1}$), the thermal conductivity of the studied minerals seems to be mediated by only phonons. Since the phononic contributions follow the $\propto T^{-1}$ dependence (solid lines in Fig. 9) in the

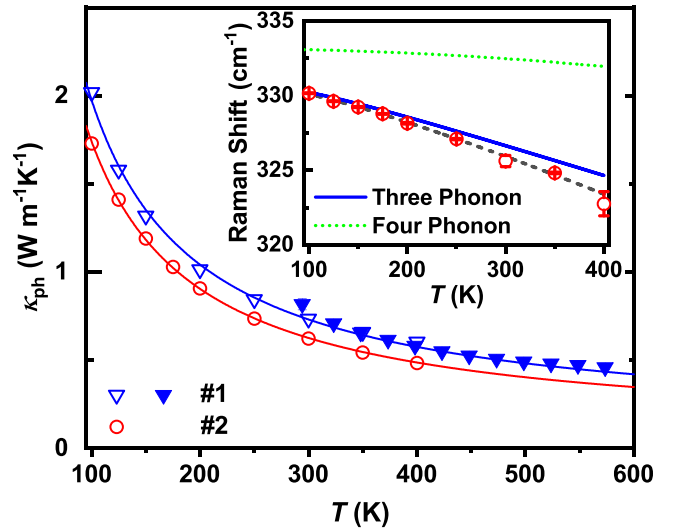


FIG. 9. Optothermal (open symbols) and LFA (filled triangles) phononic thermal conductivities for PbCuSbS_3 . Lines represent the fits to $\kappa_{\text{ph}} \propto T^{-1}$. Inset: temperature dependence of the Raman shift (red circles) for sample #2 together with fits to Klemens-Balkanski model for different scattering mechanisms of optical phonons.

temperature range 100–600 K, the phonon-phonon scattering is dominated by *umklapp* processes.

To further evaluate anharmonic phonon-phonon interactions and phonon scattering mechanisms we analyzed the temperature dependence of the Raman shift (Fig. 9 inset) applying the Klemens-Balkanski model [87]. It allows to separate the scattering of optical phonons, which are Raman active, into three-phonon and four-phonon decay mechanisms. The model is described according to Eq. (6),

$$W = W_0 + A \left[1 + \frac{2}{e^m - 1} \right] + B \left[1 + \frac{3}{e^n - 1} + \frac{3}{(e^n - 1)^2} \right] \quad (6)$$

where W_0 is the intrinsic Raman frequency, A and B anharmonic constants corresponding to three-phonon and four-phonon processes, respectively and with $m = \hbar W_0 / 2k_B T$ and $n = \hbar W_0 / 3k_B T$. The parameters of the fits to Eq. (6) (Fig. 9 inset) are collected in Table V. Simulated curves assuming $A = 0$ (i.e., four-phonon decay mechanism only) and $B = 0$ (i.e., three-phonon process only) are given in Fig. 9 (inset) by green-dotted and blue line, respectively. They, together with the percentage values given in Table V, clearly indicate the dominance of three-phonon decay mechanism. Such dominance is typical in the majority of materials. Recent theoretical studies on three and four phonon scattering

TABLE V. Raman frequency and anharmonic constants from fits of Raman shift in natural bournonites to the Klemens-Balkanski model together with estimated three-phonon contribution.

Sample	W_0 (cm $^{-1}$)	A (cm $^{-1}$)	B (cm $^{-1}$)	$\frac{A}{A+B} \times 100\%$
#1	332.4(3)	-1.77(30)	-0.14(4)	~ 93
#2	333.2(3)	-2.48(30)	-0.06(4)	~ 98

rates have shown that the latter strongly reduce the thermal conductivity of materials having phonon band gap (e.g., BAs). On the other hand, for materials having no phonon band gap (e.g., Si and diamond) three phonon scattering predicts well the thermal conductivity at low temperatures ($T < 600$ K) [88]. However, at sufficiently high temperatures, four-phonon scattering significantly contributes. Thus the presence of four-phonon scattering might be also a factor for the observed reduced $\kappa(T)$.

To further analyze the low $\kappa(T)$ in the studied minerals we used theoretically calculated elastic constants (C_{ij}) to obtain the bulk ($B \approx 174$ GPa), shear ($G \approx 91$ GPa), and Young's ($E \approx 2.6$ GPa) moduli (for details see sup. Inf.). Having them and the density of the compound (Table I), the transversal ($v_t \approx 3964$ m s⁻¹), longitudinal ($v_l \approx 7136$ m s⁻¹), and average ($v_m \approx 4415$ m s⁻¹) wave velocities could be determined from the Eqs. (7), (8), and (9), respectively,

$$v_t = \left[\frac{G}{d} \right]^{1/2}, \quad (7)$$

$$v_l = \left[\frac{B + \frac{4G}{3}}{d} \right]^{-1/3}, \quad (8)$$

$$v_m = \left[\frac{1}{3} \left(\frac{2}{v_t^3} + \frac{1}{v_l^3} \right) \right]^{-1/3}. \quad (9)$$

Further, the temperature dependencies of the Grüneisen parameter was calculated from the formula $\gamma_G = \alpha_V v_m^2 c_p^{-1}$. Herein, $\alpha_V(T) = 1/V(T)(dV/dT)$ is the experimentally measured volumetric thermal expansion coefficient [8], which was obtained from the fit of the temperature dependence of the unit cell volume (its increments are plotted in inset to Fig. 1). The obtained γ_G values vary in the range of 4.8–3.2 and thus, are much larger than $\gamma_G = 1$ –2 normally observed for semiconducting materials [21]. These large Grüneisen parameters indicate a significant phonon anharmonicity in bournonite [15], which is comparable to those in SnSe: a material with the best known TE performance nowadays [16].

The temperature dependence of the phonon mean free path (l_{ph}) (Fig. 10) is obtained by analyzing the thermal conductivity within the kinetic theory, where it is defined as $\kappa_{ph} = (c_p v_m l_{ph})/3$ [1,89]. The observed values are in the same order of magnitude as those of UCPs (Table I) and above ~ 125 K phonons should be scattered within the unit cell (Fig. 10). Similar situation is reported in some ceramics [90]. On one hand the extremely small mean free path could indicate a strong scattering of phonons and thus, corroborate a low κ . Such a consideration is widely discussed in the literature [1,2,7,9,17,90,91]. However, on the other hand, the phonons are the excitations of the entire lattice by definition and their scattering within a unit cell makes less sense. Obviously, the continuous and semiclassical kinetic theory, within which all these results were obtained, where phonons are not considered as quantum mechanical quasiparticles could lead to an inaccurate description of the extremely low thermal conductivities.

The temperature dependence of the relative heat flux $\Delta T/T_C = [T_H - T_C]/T_C$ was estimated from the local temperature rise (T_H) induced by the laser and the bulk temperature (T_C) from OTR method. Knowing this parameter the dom-

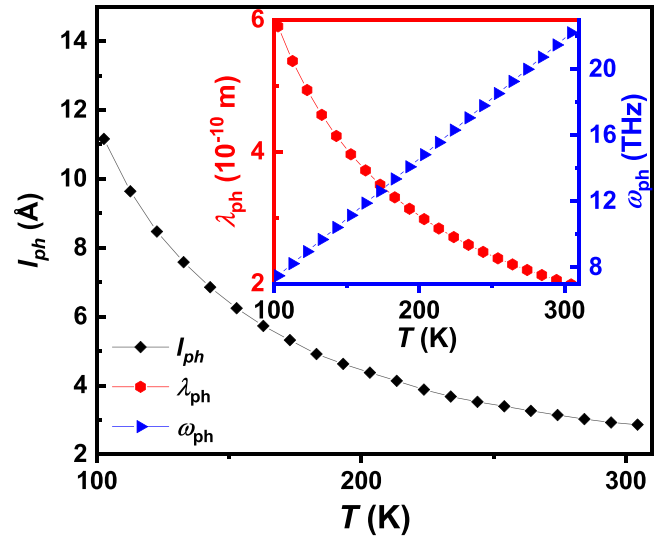


FIG. 10. Temperature dependence of the calculated phonon mean free path for PbCuSbS₃ (sample #1). Inset: Temperature dependencies of dominant phonon wavelength (λ_{ph}) and dominant phonon frequency (ω_{ph}).

inant coefficient for a 3D-material $\alpha_{3D} \propto e^{-\Delta T/T_c} \approx 3.5$ is determined as proposed in [92]. Hence, the temperature dependencies of dominant phonons' wavelength $\lambda_{ph} = h v_m (\alpha_{3D} k_B T)^{-1}$ and frequency $\omega_{ph} = v_m \lambda_{ph}^{-1}$ have been calculated. They are referred as dominant, since their values are representative of the maximum peak located in the PDOS [2]. As it is visible in Fig. 10 (inset), ω_{ph} is well above 3–5 THz (average upper limit for acoustic modes) in the whole studied temperature range, which indicates κ_{ph} to be mainly mediated by optical phonons. Further, these are known to possess a rather small group velocity due to their antiphase movement. Being strongly scattered on the acoustic phonons, the optical ones are not effective for heat transport [7].

IV. CONCLUSIONS

Optical microscopy, energy dispersive x-ray spectroscopy (EDXS), and powder x-ray diffraction (XRD) revealed natural poly- and single crystalline bournonites PbCuSbS₃ originating from mines in Neudorf im Harz (Germany) (sample #1) and Vibora (Bolivia) (sample #2) to be single phase materials whereas chemical analysis indicated them to contain minor (<1 wt.%) As and Fe impurities, respectively. These findings allowed us to consider these minerals as model systems for the comparison of the physical properties of PbCuSbS₃ of different origins.

The orthorhombic noncentrosymmetric crystal structure known for bournonite is confirmed by refinements of single crystal and powder XRD data obtained for sample #2. Comparison of the structural arrangement of PbCuSbS₃ with those of simple minerals as galena (PbS), stibnite (Sb₂S₃), and chalcopyrite (CuFeS₂) as well as with ionic radii of Pb²⁺, Cu⁺, Sb³⁺, and S²⁻ would indicate correspondingly oxidation states for all ions with the exception of lead. To get more insight into the atomic interactions, a combined spectroscopic-theoretical study including thorough analysis

of the chemical bonding situation in bournonite is required. Bournonite crystal structure is also characterized by large atomic displacement parameters for Cu and Pb atoms hinting towards their possible rattling.

The electronic structure performed within the density functional theory with the generalized gradient approximation (DFT-GGA) indicated the Pb-6*p*, Cu-4*s*, and Sb-5*p* states to be situated in the conduction band and thus to be almost depopulated. This study showed PbCuSbS₃ to be a direct semiconductor with an transport energy gap $E_g \approx 0.5$ eV and an optical one $E_g^{\text{Opt}} \approx 1.49$ eV.

The temperature dependent measurements of the magnetic susceptibility (χ) and specific heat capacity (c_p) indicated both mineral specimens to be weak Pauli paramagnets and their Sommerfeld coefficients (γ) of the electronic c_p are obviously originating from minor metallic impurities. Moreover, heat capacity measurements revealed the presence of low-energy optical phonons [i.e., maxima in $c_p/T^3(T)$ presentation], hallmarks of a “rattling” effect. The maxima could be successfully described assuming two Debye and two Einstein contributions. The latter would be in agreement with presence of two sorts of rattlers (i.e., Cu and Pb atoms). Additionally, the obtained characteristic Einstein temperatures are comparable to those deduced from the atomic displacement parameters of those atoms.

The Raman spectroscopy confirmed the studied bournonites to be of identical compositions and of the same high quality. This allowed to resolve some stretching (i.e., Sb-S at 324 cm⁻¹ and 339 cm⁻¹) and bending (S-Sb-S at 275 cm⁻¹ and 292 cm⁻¹) modes, whereas a broad region between 150–250 cm⁻¹ (~5–8 THz) comprehend a larger amount of modes, which can not be ascribed.

The fit of the ellipsometric spectra allowed to determine the real and imaginary parts of the dielectric functions, which were in good agreement with the theoretical calculations. Further determination of the energy dependencies of the absorption coefficients and their projection to zero indicated energy gaps of 1.83 eV, 1.69 eV, and 1.49 eV for samples #1, #2, and theory, respectively. The enhanced value of E_g for specimen #1 is explained by the fluid inclusions observed on its surface.

The electrical resistivity for both bournonites is high (≥ 100 Ω m) and decreases with increasing temperature as $\rho \propto e^{1/T}$ confirming the semiconducting-like behavior. The E_g^ρ values deduced from the Arrhenius plot close to room temperature are similar to those observed in our electronic calculations, representing the electronic transport band gap.

The natural specimens revealed a rather high Seebeck coefficient S of few hundreds of $\mu\text{V K}^{-1}$. The negative sign of $S(T)$ implies electrons to be the charge carriers in the studied minerals. Since both $|S|$ and ρ are inversely proportional to the charge carrier concentration, the latter is low in PbCuSbS₃. Consequently, the power factor, estimated as $PF = S^2 T \rho^{-1}$ and characterizing the performance of the thermoelectric materials is nearly three orders of magnitude lower than those of the state-of-the-art materials.

Analysis of the temperature dependencies of the thermal conductivity $\kappa(T)$ obtained by LFA and optothermal Raman (OTR) technique indicated heat transport in the studied samples to be weak and mediated only by phonons (i.e., κ_{ph}). Since κ_{ph} follows the $\propto T^{-1}$ dependence, the phonon-phonon scattering is mainly due to *umklapp* processes. Further analysis of the temperature dependence of the Raman shift within the Klemens-Balkanski model allowed to separate the scattering of the optical phonons into three-phonon and four-phonon decay mechanisms, and confirmed the former one to be dominating. Additionally, the theoretically calculated elastic constants, allowed us to obtain the sound velocity and further estimate the Grüneisen parameter $\gamma_G = 4.8$ –3.2 and the temperature dependence of the phonon-mean free path l_{ph} . The values of the former are by a factor of ~2–3 higher than those of simple semiconducting materials and indicated a significant phonon anharmonicity in bournonite, which is compatible again with low $\kappa(T)$. And finally, we found the dominant phonons' frequency ω_{ph} in bournonite to be well above 3–5 THz, thus confirming mediation of κ_{ph} by optical phonons. The latter are known to possess rather low group velocity due to their antiphase movement, to be not effective for heat transport and to strongly scatter the acoustic ones.

ACKNOWLEDGMENTS

This work was performed within the DFG (Deutsche Forschungsgemeinschaft) Project No. 441856638. The DynaCool-12 system was acquired within the DFG Project No. 422219907. The authors thank G. Heide and A. Masanek for providing us the sample #1, U. Burkhardt, M. Eckert, S. Kostmann and U. Fischer for metallographic preparation and analysis; H. Borrmann, S. Hückmann, C. Hennig and V. Levystky for x-ray diffraction experiments and discussions; G. Aufermann for chemical analysis and Yu. Grin for his steady support of this work.

-
- [1] E. S. Toberer, L. L. Baranowski, and C. Dames, *Annu. Rev. Mater. Res.* **42**, 179 (2012).
- [2] D. R. Clarke, *Surf. Coat. Technol.* **163-164**, 67 (2003).
- [3] A. Polman, M. Knight, E. C. Garnett, B. Ehrler, and W. C. Sinke, *Science* **352**, aad4424 (2016).
- [4] G. S. Nolas, J. Sharp, and J. Goldsmid, *Thermoelectrics: Basic Principles and New Materials Developments*, Vol. 45 (Springer Science & Business Media, New York, 2001).
- [5] L. E. Bell, *Science* **321**, 1457 (2008).
- [6] J. Sommerlatte, K. Nielsch, and H. Bottner, *Phys. J.* **6**, 35 (2007).
- [7] T. M. Tritt, *Thermal Conductivity: Theory, Properties, and Applications* (Springer Science & Business Media, New York, 2005).
- [8] R. Gross, A. Marx, D. Einzel, and S. Geprägs, *Festkörperphysik: Aufgaben und Lösungen* (De Gruyter, Berlin, 2018).
- [9] X. Qian, J. Zhou, and G. Chen, *Nat. Mater.* **20**, 1188 (2021).

- [10] Y. Cheng, M. Nomura, S. Volz, and S. Xiong, *J. Appl. Phys.* **130**, 040902 (2021).
- [11] M. Li, Y. Tsurimaki, Q. Meng, N. Andrejevic, Y. Zhu, G. D. Mahan, and G. Chen, *New J. Phys.* **20**, 023010 (2018).
- [12] T. Feng and X. Ruan, *Phys. Rev. B* **97**, 045202 (2018).
- [13] A. Katre, J. Carrete, B. Dongre, G. K. H. Madsen, and N. Mingo, *Phys. Rev. Lett.* **119**, 075902 (2017).
- [14] M. Simoncelli, N. Marzari, and F. Mauri, *Nat. Phys.* **15**, 809 (2019).
- [15] G. A. Slack, *J. Phys. Chem. Solids* **34**, 321 (1973).
- [16] L.-D. Zhao, S.-H. Lo, Y. Zhang, H. Sun, G. Tan, C. Uher, C. Wolverton, V. P. Dravid, and M. G. Kanatzidis, *Nature (London)* **508**, 373 (2014).
- [17] E. Osei-Agyemang, C. E. Adu, and G. Balasubramanian, *npj Comput. Mater.* **5**, 1 (2019).
- [18] A. Fischer, E.-W. Scheidt, W. Scherer, D. E. Benson, Y. Wu, D. Eklöf, and U. Häussermann, *Phys. Rev. B* **91**, 224309 (2015).
- [19] C. Bourgès, P. Lemoine, O. I. Lebedev, R. Daou, V. Hardy, B. Malaman, and E. Guilmeau, *Acta Mater.* **97**, 180 (2015).
- [20] M. K. Jana, K. Pal, A. Warankar, P. Mandal, U. V. Waghmare, and K. Biswas, *J. Am. Chem. Soc.* **139**, 4350 (2017).
- [21] C. Chang and L.-D. Zhao, *Mater. Today Phys.* **4**, 50 (2018).
- [22] Y. Grin, *J. Solid State Chem.* **274**, 329 (2019).
- [23] S. Lee, K. Esfarjani, T. Luo, J. Zhou, Z. Tian, and G. Chen, *Nat. Commun.* **5**, 3525 (2014).
- [24] J. W. Anthony, R. A. Bideaux, K. Bladh, and M. C. Nichols, *Handbook of Mineralogy: Elements, Sulfides, sulfosalts* (Mineral Data Publishing, Tucson, 1990).
- [25] C. S. Hurlbut, E. S. Dana, and W. E. Sharp, *Dana's Minerals and How to Study Them* (John Wiley & Sons, Hoboken, NJ, 1998).
- [26] A. Edenharter and W. Nowacki, *Zeitschrift für Kristallographie* **131**, 397 (1970).
- [27] R. Alieva, S. Bairamova, V. Ragimova, O. Aliev, and M. Bagieva, *Inorg. Mater.* **46**, 703 (2010).
- [28] Y. Dong, A. R. Khabibullin, K. Wei, J. R. Salvador, G. S. Nolas, and L. M. Woods, *Chem. Phys. Chem.* **16**, 3264 (2015).
- [29] A. Faghaninia, G. Yu, U. Aydemir, M. Wood, W. Chen, G.-M. Rignanese, G. J. Snyder, G. Hautier, and A. Jain, *Phys. Chem. Chem. Phys.* **19**, 6743 (2017).
- [30] S. K. Wallace, K. L. Svane, W. P. Huhn, T. Zhu, D. B. Mitzi, V. Blum, and A. Walsh, *Sustainable Energy Fuels* **1**, 1339 (2017).
- [31] C. Tablero, *Theor. Chem. Acc.* **135**, 1 (2016).
- [32] K. Wei, J. Martin, J. R. Salvador, and G. S. Nolas, *Cryst. Growth Des.* **15**, 3762 (2015).
- [33] K. M. Koskela, B. C. Melot, and R. L. Brutchey, *J. Am. Chem. Soc.* **142**, 6173 (2020).
- [34] Y. Liu, B. Yang, M. Zhang, B. Xia, C. Chen, X. Liu, J. Zhong, Z. Xiao, and J. Tang, *Nano Energy* **71**, 104574 (2020).
- [35] M. Zhang, C. Wang, C. Chen, and J. Tang, *Front. Optoelectron.* **14**, 450 (2021).
- [36] Y. T. Alharbi, F. Alam, K. Parvez, M. Missous, and D. J. Lewis, *Inorg. Chem.* **60**, 13691 (2021).
- [37] S. Bairamova, M. Bagieva, S. Agapashaeva, and O. Aliev, *Inorg. Mater.* **47**, 345 (2011).
- [38] E. Zuñiga-Puelles, R. Cardoso-Gil, M. Bobnar, I. Veremchuk, C. Himcinschi, C. Hennig, J. Kortus, G. Heide, and R. Gumeniuk, *Dalton Trans.* **48**, 10703 (2019).
- [39] E. Zuñiga-Puelles, R. Cardoso-Gil, M. Bobnar, I. Veremchuk, G. Heide, and R. Gumeniuk, *J. Phys. Chem. Solids* **150**, 109809 (2021).
- [40] X. Lu, D. T. Morelli, Y. Xia, F. Zhou, V. Ozolins, H. Chi, X. Zhou, and C. Uher, *Adv. Energy Mater.* **3**, 342 (2013).
- [41] P. Wyżga, M. Bobnar, C. Hennig, A. Leithe-Jasper, T. Mori, and R. Gumeniuk, *Z. Anorg. Allg. Chem.* **643**, 858 (2017).
- [42] H. M. Ferreira, E. B. Lopes, J. F. Malta, L. M. Ferreira, M. H. Casimiro, L. Santos, M. F. Pereira, and A. P. Gonçalves, *PeerJ Mater. Sci. Chem.* **1**, e2 (2019).
- [43] P. Wyżga, I. Veremchuk, C. Himcinschi, U. Burkhardt, W. Carrillo-Cabrera, M. Bobnar, C. Hennig, A. Leithe-Jasper, J. Kortus, and R. Gumeniuk, *Dalton Trans.* **48**, 8350 (2019).
- [44] P. Wyżga, W. Carrillo-Cabrera, L. Akselrud, I. Veremchuk, J. Wagler, C. Hennig, A. A. Tsirlin, A. Leithe-Jasper, E. Kroke, and R. Gumeniuk, *Dalton Trans.* **49**, 15903 (2020).
- [45] P. Wyżga, S. Grimm, V. Garbe, E. Zuñiga-Puelles, C. Himcinschi, I. Veremchuk, A. Leithe-Jasper, and R. Gumeniuk, *J. Mater. Chem. C* **9**, 4008 (2021).
- [46] P. Wyżga, I. Veremchuk, M. Bobnar, P. Koželj, S. Klenner, R. Pöttgen, A. Leithe-Jasper, and R. Gumeniuk, *Chem. Eur. J.* **26**, 5245 (2020).
- [47] P. Wyżga, I. Veremchuk, M. Bobnar, C. Hennig, A. Leithe-Jasper, and R. Gumeniuk, *Z. Anorg. Allg. Chem.* **646**, 1091 (2020).
- [48] P. Wyżga, I. Veremchuk, P. Koželj, A. Leithe-Jasper, and R. Gumeniuk, *J. Phys. Chem. Solids* **152**, 109984 (2021).
- [49] STOE Powder Software, WinXPow (version 2), Darmstadt, STOE and Cie GmbH, 2001, <https://www.stoe.com/product/software-powder-xrd/>.
- [50] CrysAlisPRO, Oxford Diffraction/Agilent Technologies UK Ltd, Yarnton, England, <https://www.rigaku.com/de/products/smc/crystalis>.
- [51] L. Akselrud and Y. Grin, *J. Appl. Crystallogr.* **47**, 803 (2014).
- [52] See Supplemental Material at <http://link.aps.org/supplemental/10.1103/PhysRevB.106.195201> for results of elastic constant calculation, of EDX and ICP-EOS analyses, crystal structure refinement, as well as Raman spectra evaluations.
- [53] J. Wilkinson, *Lithos* **55**, 229 (2001).
- [54] H. Malekpour and A. A. Balandin, *J. Raman Spectrosc.* **49**, 106 (2018).
- [55] S. Périchon, V. Lysenko, B. Remaki, D. Barbier, and B. Champagnon, *J. Appl. Phys.* **86**, 4700 (1999).
- [56] B. Stoib, S. Filser, J. Stötzel, A. Greppmair, N. Petermann, H. Wiggers, G. Schierning, M. Stutzmann, and M. S. Brandt, *Semicond. Sci. Technol.* **29**, 124005 (2014).
- [57] K. Koepf and H. Eschrig, *Phys. Rev. B* **59**, 1743 (1999).
- [58] J. P. Perdew and Y. Wang, *Phys. Rev. B* **45**, 13244 (1992).
- [59] P. Giannozzi, S. Baroni, N. Bonini, M. Calandra, R. Car, C. Cavazzoni, D. Ceresoli, G. L. Chiarotti, M. Cococcioni, I. Dabo *et al.*, *J. Phys.: Condens. Matter* **21**, 395502 (2009).
- [60] A. Dal Corso, *Computational Mater. Sci.* **95**, 337 (2014).
- [61] J. P. Perdew, K. Burke, and M. Ernzerhof, *Phys. Rev. Lett.* **78**, 1396 (1997)[erratum].
- [62] H. J. Monkhorst and J. D. Pack, *Phys. Rev. B* **13**, 5188 (1976).
- [63] P. Ravindran, L. Fast, P. A. Korzhavyi, B. Johansson, J. Wills, and O. Eriksson, *J. Appl. Phys.* **84**, 4891 (1998).
- [64] S. Kharbish, G. Gierster, and A. Beran, *N. Jb. Miner. Abh.* **187**, 159 (2010).

- [65] S. Hall and J. Stewart, *Acta Cryst. B* **29**, 579 (1973).
- [66] P. Bayliss and W. Nowacki, *Z. Kristallog.* **135**, 308 (1972).
- [67] R. D. Shannon, *Acta Crystallogr. Sect. A* **32**, 751 (1976).
- [68] Y. Noda, K. Masumoto, S. Ohba, Y. Saito, K. Toriumi, Y. Iwata, and I. Shibuya, *Acta Cryst. C* **43**, 1443 (1987).
- [69] A. Spek, *J. Appl. Crystallogr.* **36**, 7 (2003).
- [70] B. J. Wuensch, *Z. Kristallog.* **119**, 437 (1964).
- [71] R. Patrick, G. Van Der Laan, D. Vaughan, and C. Henderson, *Phys. Chem. Miner.* **20**, 395 (1993).
- [72] R. Chevrel, M. Sergent, and J. Prigent, *Mater. Res. Bull.* **9**, 1487 (1974).
- [73] L.-D. Zhao, V. P. Dravid, and M. G. Kanatzidis, *Energy Environ. Sci.* **7**, 251 (2014).
- [74] A. P. Gonçalves and C. Godart, *Eur. Phys. J. B* **87**, 1 (2014).
- [75] J. P. Perdew, *Int. J. Quantum Chem.* **28**, 497 (1985).
- [76] M. Städele, M. Moukara, J. A. Majewski, P. Vogl, and A. Görling, *Phys. Rev. B* **59**, 10031 (1999).
- [77] S. W. Goh, A. N. Buckley, R. N. Lamb, R. A. Rosenberg, and D. Moran, *Geochim. Cosmochim. Acta* **70**, 2210 (2006).
- [78] G. A. Bain and J. F. Berry, *J. Chem. Educ.* **85**, 532 (2008).
- [79] G. S. Nolas, ed., *The Physics and Chemistry of Inorganic Clathrates* (Springer Netherlands, Dordrecht, 2014).
- [80] C. Uher, in *Recent Trends in Thermoelectric Materials Research I*, Vol. 69 of *Semiconductors and Semimetals* (Elsevier, Amsterdam, 2001), pp. 139–253.
- [81] R. Gumeniuk, in *Handbook on the Physics and Chemistry of Rare Earths* (Elsevier, Amsterdam, 2018), Vol. 54, pp. 43–143.
- [82] M. Beekman, W. Schnelle, H. Borrmann, M. Baitinger, Y. Grin, and G. S. Nolas, *Phys. Rev. Lett.* **104**, 018301 (2010).
- [83] Y. Ikeuchi, H. Takatsu, C. Tassel, C. M. Brown, T. Murakami, Y. Matsumoto, Y. Okamoto, and H. Kageyama, *Inorg. Chem.* **58**, 6790 (2019).
- [84] S. Kharbish, E. Libowitzky, and A. Beran, *Eur. J. Mineral.* **19**, 567 (2007).
- [85] S. Kharbish, E. Libowitzky, and A. Beran, *Eur. J. Mineral.* **21**, 325 (2009).
- [86] M. Wolf, R. Hinterding, and A. Feldhoff, *Entropy* **21**, 1058 (2019).
- [87] M. Balkanski, R. F. Wallis, and E. Haro, *Phys. Rev. B* **28**, 1928 (1983).
- [88] T. Feng, L. Lindsay, and X. Ruan, *Phys. Rev. B* **96**, 161201(R) (2017).
- [89] O. Bourgeois, D. Tainoff, A. Tavakoli, Y. Liu, C. Blanc, M. Boukhari, A. Barski, and E. Hadji, *C. R. Phys.* **17**, 1154 (2016).
- [90] R. Wu, W. Pan, X. Ren, C. Wan, Z. Qu, and A. Du, *Acta Mater.* **60**, 5536 (2012).
- [91] Y. Xiao, C. Chang, Y. Pei, D. Wu, K. Peng, X. Zhou, S. Gong, J. He, Y. Zhang, Z. Zeng, Z. Zeng, and L.-D. Zhao, *Phys. Rev. B* **94**, 125203 (2016).
- [92] A. Ramiere, S. Volz, and J. Amrit, *AIP Adv.* **7**, 015017 (2017).